




Cite this: DOI: 10.1039/d5ta03974f

# Zinc-ion storage mechanisms in poly(*o*-phenylenediamine): insights into structural advantages and electrochemical performance†

Yi Xu,<sup>a</sup> Xian-Zhong Tang,<sup>\*a</sup> Xingchen Xie,<sup>a</sup> Ni Wang<sup>ab</sup> and Sridhar Komarneni <sup>\*b</sup>

Zinc-ion organic batteries (ZOBs) are emerging as a viable energy storage alternative, valued for their superior safety features and economic viability. Poly(*o*-phenylenediamine) (PoPDA), recognized for its cost efficiency, has emerged as a potential cathode candidate in ZOB systems. However, the rapid decline in specific capacity and the limited cycle life of PoPDA-based electrodes have hindered the advancement and utilization of these electrodes. In this research, high molecular weight poly(*o*-phenylenediamine) (PoPDA<sub>H</sub>) was synthesized through *in situ* chemical oxidative polymerization to serve as an efficient cathode material for zinc-ion organic batteries (ZOBs). This composite exhibited a high capacity of 258 mAh g<sup>-1</sup> at 0.1 A g<sup>-1</sup> and retained 97.4% of its capacity after 2000 cycles at 1.0 A g<sup>-1</sup>, emphasising the significant potential of PoPDA<sub>H</sub> in the pursuit of high-performance ZOB electrode materials.

Received 16th May 2025  
Accepted 22nd July 2025

DOI: 10.1039/d5ta03974f

[rsc.li/materials-a](https://rsc.li/materials-a)

## 1. Introduction

Aqueous zinc-ion batteries have received significant attention due to their high theoretical specific capacity, low redox potential, improved safety, and environmental benefits. These characteristics make them an extremely promising choice for prospective large-scale energy storage systems.<sup>1,2</sup> To date, a significant proportion of research has centered on identifying cathode materials for zinc-ion batteries that offer high energy density and extended lifespan.<sup>3</sup> Various manganese-<sup>4</sup> and vanadium-based oxides/sulfides<sup>5</sup> with tunnel/layered structures, as well as Prussian blue analogs,<sup>6</sup> have been utilized as cathode materials. However, these conventional inorganic cathode materials are characterized by severe structural collapse and pulverization, which often results in rapid capacity decay and poor cycling performance during charge/discharge processes. Moreover, these materials frequently contain toxic or polluting elements, which contradicts the green development philosophy of large-scale energy storage systems.

Contrast to conventional inorganic electrode materials, organic electrode materials (OEMs) made up of plentiful light elements such as C, H, O, and N are considered as promising candidates for building future green and sustainable energy

storage devices. The rearrangement of chemical bonds during energy storage in OEMs can avoid the severe structural changes often associated with ion insertion/extraction in inorganic electrode materials. However, organic small molecules containing quinone and pyrazine units exhibit only modest solubility in aqueous electrolytes, resulting in suboptimal cyclic stability.<sup>7–10</sup> A comprehensive solution to this challenge entails the synthesis of larger molecules, particularly polymers, and the construction of strong  $\pi$ - $\pi$  stacking interactions between molecules to enhance the insolubility of organic materials. Numerous studies have concentrated on creating quinone-based polymers<sup>11–14</sup> and covalent organic frameworks (COFs)<sup>15–20</sup> as cathode materials for ZOBs, which have demonstrated notable electrochemical performance. However, the synthesis process is intricate and costly, which hinders their large-scale application.

Polyaniline (PANI), an electrode material that has been the subject of much research due to its excellent conductivity and well-established synthesis process, has found wide application in various battery systems.<sup>21–25</sup> In aqueous metal-ion batteries, PANI has been employed as an efficient cathode, a property attributable to its abundant active sites and excellent conductivity.<sup>26–29</sup> Inspired by this, poly(*o*-phenylenediamine) (PoPDA) synthesized at room temperature has been confirmed as a cathode material for ZOBs.<sup>30</sup> Despite its initial capacity being high, its cycling stability is poor, possibly related to its low degree of polymerization, and research on its reaction mechanism is lacking. Consequently, there is a necessity to explore the synthesis conditions of PoPDA and conduct further research on its applications. Additionally, Zn<sup>2+</sup> demonstrates slow diffusion within organic cathodes, a limitation that can be overcome by

<sup>a</sup>School of Materials and Energy, University of Electronic Science and Technology of China, Chengdu 611731, China

<sup>b</sup>Materials Research Institute and Department of Ecosystem Science and Management, 204 Energy and the Environment Laboratory, The Pennsylvania State University, University Park, PA 16802, USA

† Electronic supplementary information (ESI) available. See DOI: <https://doi.org/10.1039/d5ta03974f>



incorporating highly conductive carbon materials, such as activated carbon, carbon nanotubes, and graphene, which enhance redox kinetics.<sup>10,31–36</sup>

In this work, we successfully synthesized polyphenylene diamine with a high molecular weight (PoPDA<sub>H</sub>). The material demonstrated a high specific capacity of 258 mAh g<sup>-1</sup> at 0.1 A g<sup>-1</sup> and retained stable electrochemical performance over 2000 cycles at 1.0 A g<sup>-1</sup>. Notably, its performance was comparable to that of nitrogen-containing heterocyclic polymers with analogous structural features. However, PoPDA<sub>H</sub> demonstrated a substantial advantage in terms of production cost and synthetic simplicity, as it was synthesized at a significantly lower cost and *via* a more straightforward method than its counterparts.

## 2. Experimental procedures

### 2.1 Materials

*o*-Phenylenediamine (*o*PDA, 99%) was purchased from TCI. Hydrochloric acid (HCl), ammonium persulfate (APS), saturated sodium chloride (NaCl), glacial acetic acid (HoAc), 30% hydrogen peroxide (H<sub>2</sub>O<sub>2</sub>), ammonia monohydrate (NH<sub>3</sub>·H<sub>2</sub>O) and hydrazine hydrazide (N<sub>2</sub>H<sub>4</sub>) were procured from Chengdu Kelong Chemical Reagent Factory. The 3 M Zn(CF<sub>3</sub>SO<sub>3</sub>)<sub>2</sub> electrolyte was obtained from Duoduo Reagent (Suzhou, China). All chemical reagents were employed directly without undergoing further purification procedures.

### 2.2 Synthesis of PoPDA<sub>L</sub>

Firstly, 1.0 g (9.25 mmol) of *o*PDA was dissolved in 92.5 mL of deionized water to prepare a 0.1 mol per L *o*PDA solution. Subsequently, 40 mL of 0.12 mol per L HCl solution and 40 mL of NaCl solution were sequentially added to the *o*PDA solution. Following this, 40 mL of 30% (v/v) H<sub>2</sub>O<sub>2</sub> was introduced to the mixture, which was then stirred vigorously. After stirring, the mixture was allowed to incubate in the dark for 24 h. The resulting solution was vacuum-filtered to remove residual solvent, and the precipitate was repeatedly washed with deionized water. Finally, the precipitate was dried in a vacuum oven at 50 °C for 24 h, yielding the polymer denoted as PoPDA<sub>L</sub>.

### 2.3 Synthesis of PoPDA<sub>H</sub>

The synthesis of PoPDA<sub>H</sub> involved chemically oxidizing *o*PDA in a 75/25 (v/v) mixture of acetic acid and water using ammonium persulfate (APS) as the oxidant. The detailed synthesis procedure is as follows: 1.0 g (9.25 mmol) of *o*PDA was mixed with 75 mL of glacial acetic acid in a 250 mL glass beaker and stirred for 30 minutes under standard conditions. In a separate container, 6.3 g (27.75 mmol) of APS was dissolved in 25 mL of deionized water (DI) to form the oxidant solution. This solution was then dripped into the monomer solution (maintaining a 1 : 3 monomer/oxidant molar ratio) at a rate of one drop every 5 seconds over a 30-minute period. The mixture was subsequently heated and refluxed at 118 °C for 72 hours. Once the reaction was complete, the solid product was collected, washed extensively with distilled water and ethanol, and dried in a vacuum

oven at 50 °C for 24 hours to produce PoPDA<sub>H</sub> as a fine solid powder with a yield of approximate 78%.

### 2.4 Material characterizations

The Elementar vario EL cube organic elemental analyzer was used for elemental composition analysis. Fourier transform infrared spectroscopy (FTIR) measurements were performed using a Bruker INVENIO R instrument. X-ray diffraction (XRD) patterns were generated with the Rigaku Ultima IV system, which utilized Cu K $\alpha$  radiation and scanned across a  $2\theta$  range of 5° to 80°. X-ray photoelectron spectroscopy (XPS) data were obtained using a Kratos AXIS Ultra DLD spectrometer equipped with an Al K $\alpha$  source. The binding energy scale for the XPS data was referenced to the C 1s peak corresponding to the neutral C–C bond at 284.8 eV. Microstructural and morphological evaluations were conducted using field-emission scanning electron microscopy (FESEM) with a Thermo Fisher Apreo 2C instrument.

### 2.5 Electrode preparation and electrochemical measurement

The cathode slurry was created by mixing the active materials, Ketjen Black (KB) and PVDF (Arkema HSV 900), in a 60 : 30 : 10 weight ratio. *N*-Methyl-2-pyrrolidone (NMP) was used as the dispersion agent. This mixture was then applied to a stainless-steel mesh current collector and dried in a vacuum oven at 80 °C for an extended period to ensure complete solvent removal. The resulting electrodes had active material loadings ranging from 1.0 to 1.5 mg cm<sup>-2</sup>. A high-purity zinc foil (99.9% purity) served as the anode, with Whatman GF/D glass microfiber filters used as the separator. Coin cells (CR2032, Clorox) were assembled in ambient conditions using a 3 M Zn(CF<sub>3</sub>SO<sub>3</sub>)<sub>2</sub> aqueous electrolyte. Electrochemical testing was performed at room temperature using a LAND CT 2001A multi-channel battery tester for constant-current cycling and galvanostatic intermittent titration (GITT). Further analyses, including cyclic voltammetry (CV) and electrochemical impedance spectroscopy (EIS), were conducted using a Wuhan CorrTest CS300 electrochemical workstation.

## 3. Results and discussion

### 3.1 Material structure characteristics

The synthetic routes for PoPDA<sub>H</sub> and PoPDA<sub>L</sub> are illustrated in Fig. 1a. *o*-Phenylenediamine (*o*PDA) was served as the monomer, with acetic acid as the solvent and ammonium persulfate (APS) acting as the oxidizing agent. Through refluxing at 118 °C for 72 hours, a brown-black powder sample, designated as PoPDA<sub>H</sub>, was obtained. For comparative purposes, a brown-red powder sample, designated as PoPDA<sub>L</sub>, was synthesized according to previously reported methods. This synthesis employed a sodium chloride/hydrochloric acid solution as the solvent and hydrogen peroxide as the oxidizing agent, with the reaction proceeding at room temperature in a dark environment for 24 hours.



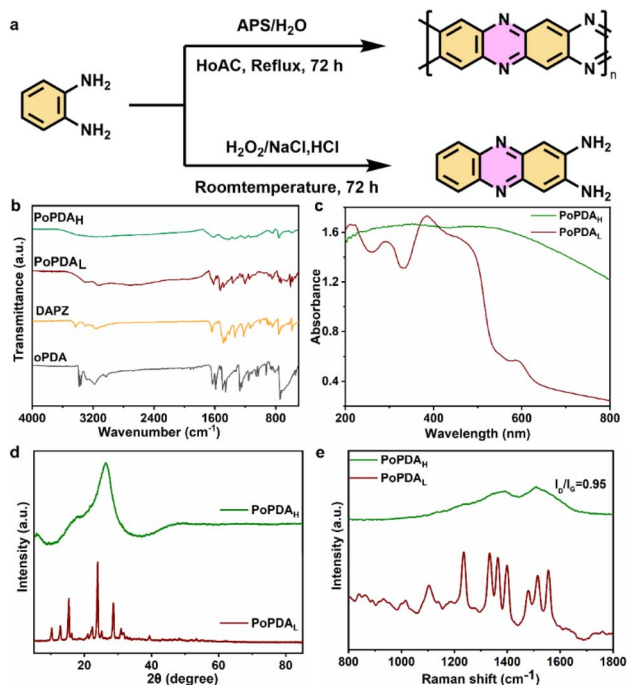


Fig. 1 (a) The synthetic procedure, (b) FTIR spectra, (c) UV-vis spectra, (d) XRD pattern and (e) Raman spectra.

To confirm the structure of the products, Fourier-transform infrared spectroscopy (FTIR) was employed to analyze the functional groups of the samples. As shown in Fig. 1b, the characteristic peaks of PoPDA<sub>L</sub> and 2,3-diaminophthalazine (DAPZ, the dimer of oPDA) exhibit high consistency. In comparison, PoPDA<sub>H</sub> displays distinguishable peaks with significant overlap and markedly weaker intensities. Notably, the broadband shape between 1700 and 900 cm<sup>-1</sup> shows substantial differences, indicating a larger molecular weight and more complex structure in PoPDA<sub>H</sub> relative to PoPDA<sub>L</sub>.

The UV-vis spectrum (Fig. 1b) shows the primary absorption band of PoPDA<sub>L</sub> at 424 nm, which is attributed to the  $\pi$ - $\pi^*$  electronic transition of the phthalazine ring system conjugated with the lone pair nitrogen of the -NH<sub>2</sub> group. In contrast, PoPDA<sub>H</sub>, due to its higher degree of polymerization, exhibits no discernible absorption features.

The supramolecular structures of PoPDA<sub>H</sub> and PoPDA<sub>L</sub> were characterized using X-ray diffraction (XRD). As depicted in Fig. 1d, PoPDA<sub>L</sub> exhibits high crystallinity, whereas PoPDA<sub>H</sub> displays an amorphous structure, indicative of its polymeric nature.

The <sup>1</sup>H NMR spectrum of PoPDA<sub>L</sub> (Fig. S1†) displays four distinct peaks at 7.90, 7.55, 6.91, and 6.27 ppm, with an atomic ratio of 1 : 1 : 1 : 2, thereby confirming the high purity of DAPZ in PoPDA<sub>L</sub>. Furthermore, the <sup>13</sup>C NMR spectrum of PoPDA<sub>L</sub> (Fig. S2†) corroborates this conclusion.

Raman spectroscopy (Fig. 1e) reveals distinct D and G band peaks for PoPDA<sub>H</sub> at 1390 and 1520 cm<sup>-1</sup>, respectively. These peaks are attributed to defects and disorder in the graphene-like structure, as well as to the in-plane vibrational bonding of sp<sup>2</sup>

carbon atoms. The presence of the D and G peaks further confirms the existence of  $\pi$ - $\pi$  interactions between molecular planes.<sup>37,38</sup> The Raman signal of PoPDA<sub>L</sub> suggests it is a low-molecular-weight compound rather than a polymeric material.

High-resolution N 1s, O 1s, and C 1s XPS spectra of PoPDA<sub>H</sub> and PoPDA<sub>L</sub> were examined, as presented in Fig. 2a-c. The N 1s spectrum can be deconvoluted into two components: a dominant =N- peak at 398.7 eV and a minor -NH<sub>2</sub>/-NH- peak at 400 eV, suggesting the presence of abundant phthalazine units. For the O 1s spectrum, PoPDA<sub>L</sub> exhibits a single peak at 533.1 eV, attributed to trace amounts of H<sub>2</sub>O, while PoPDA<sub>H</sub> shows an additional peak at 531.5 eV corresponding to C=O, likely originating from residual carboxyl groups. Notably, the  $\pi$ - $\pi^*$  satellite peak at approximately 291 eV is exclusively observed in PoPDA<sub>H</sub>, indicating the existence of a conjugated system and  $\pi$ - $\pi$  stacking.

Thermogravimetric analysis (TGA, Fig. 2d) demonstrates that the monomer oPDA decomposes completely at 240 °C, PoPDA<sub>L</sub> initiates decomposition around 230 °C, and PoPDA<sub>H</sub> experiences approximately 5 wt% mass loss below 150 °C, attributed to the loss of absorbed water. Beyond 400 °C, PoPDA<sub>H</sub> exhibits substantial mass loss, confirming its polymeric nature.

Scanning electron microscopy (SEM) and transmission electron microscopy (TEM) were employed to investigate the morphologies of PoPDA<sub>H</sub>. As depicted in Fig. 2e, S3 and 4† PoPDA<sub>H</sub> exhibits irregularly shaped plate-like aggregates with dimensions on the order of hundreds of nanometers. Whereas, PoPDA<sub>L</sub> displays a particulate morphology, as evidenced by Fig. 2f.

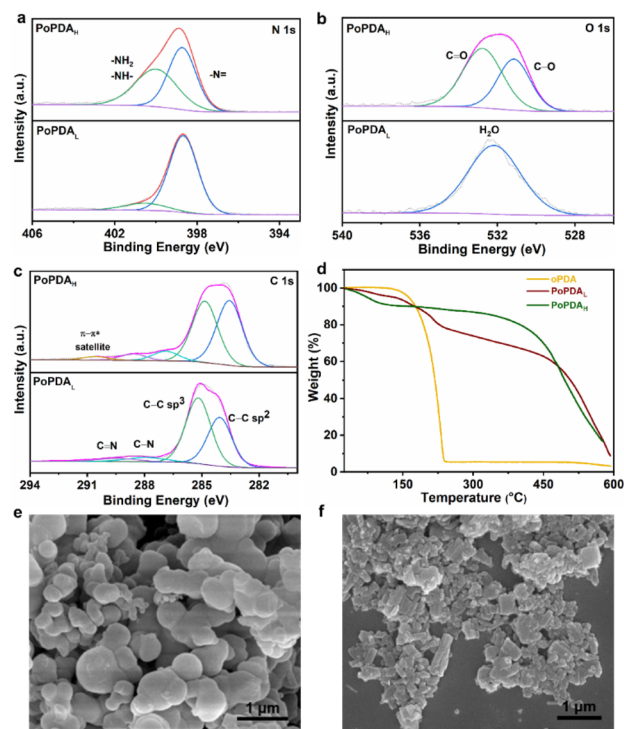


Fig. 2 XPS spectra of (a) N 1s, (b) O 1s, (c) C 1s, (d) TG curves (air atmosphere, 10 °C min<sup>-1</sup>) and SEM images of (e) PoPDA<sub>H</sub> and (f) PoPDA<sub>L</sub>.





### 3.2 Electrochemical properties

The  $\text{Zn}^{2+}$  storage performance was evaluated using coin cells fabricated with a 3.0 M  $\text{Zn}(\text{CF}_3\text{SO}_3)_2$  electrolyte. As shown in Fig. 3a and b,  $\text{PoPDA}_\text{L}$  exhibits a flat charge–discharge platform, with capacity continuously declining from the second cycle onward, indicating significant dissolution in the electrolyte and capacity fading issues. In contrast, the galvanostatic charge–discharge (GCD) curves of  $\text{PoPDA}_\text{H}$  electrodes display sloping charge–discharge profiles, with capacities stabilizing at 258  $\text{mAh g}^{-1}$  from the second to tenth cycle at 0.1  $\text{A g}^{-1}$ . Compared to  $\text{PoPDA}_\text{L}$ ,  $\text{PoPDA}_\text{H}$  demonstrates markedly enhanced electrochemical stability, attributed to its pronounced  $\pi$ – $\pi$  conjugated structure, which substantially reduces electrolyte solubility while enhancing electrochemical activity.

The Fig. 3c illustrates the rate performance of the  $\text{PoPDA}_\text{L}$  and  $\text{PoPDA}_\text{H}$  electrode under various current densities. Initially,  $\text{PoPDA}_\text{H}$  exhibits an average capacity of 252  $\text{mAh g}^{-1}$  during the first 10 cycles at 0.1  $\text{A g}^{-1}$ . The capacity retention rates at 0.2, 0.5, 1.0, 2.0, and 5.0  $\text{A g}^{-1}$  are 92%, 85%, 74%, 62%, 54%, and 44%, respectively, demonstrating excellent rate capability. However, the capacity retention rates of the  $\text{PoPDA}_\text{L}$  electrode are significantly lower than those of  $\text{PoPDA}_\text{H}$ , at 75.7%, 73.4%, 58.5%, 46.8%, and 25.4% under the corresponding current densities. This indicates that the two electrodes employ distinct charge storage mechanisms, highlighting the crucial role of  $\text{PoPDA}_\text{H}$ 's high molecular weight in enhancing charge storage capacity. Based on these findings, the cycling stability of the two  $\text{PoPDA}$  electrodes was compared at a low current density of 0.2  $\text{A g}^{-1}$  (Fig. 3d). The  $\text{PoPDA}_\text{L}$  electrode exhibits a maximum

reversible capacity of 215  $\text{mAh g}^{-1}$ , while the  $\text{PoPDA}_\text{H}$  electrode achieves a slightly higher maximum reversible capacity of 220  $\text{mAh g}^{-1}$ . During the initial 100 cycles, the reversible capacity of  $\text{PoPDA}_\text{L}$  undergoes rapid decay, whereas  $\text{PoPDA}_\text{H}$  maintains a stable capacity trend. After 100 cycles, both electrodes reach capacity stabilization. Ultimately,  $\text{PoPDA}_\text{H}$  and  $\text{PoPDA}_\text{L}$  electrodes deliver reversible capacities of 220 and 113  $\text{mAh g}^{-1}$ , respectively. Furthermore, the long-term stability of  $\text{PoPDA}_\text{H}$  and  $\text{PoPDA}_\text{L}$  electrodes was evaluated at a current density of 1.0  $\text{A g}^{-1}$  (Fig. 3e). The  $\text{PoPDA}_\text{H}$  electrode maintains a reversible capacity of 159  $\text{mAh g}^{-1}$  after 2000 cycles with near-100% coulombic efficiency, demonstrating minimal capacity decay. In contrast, the  $\text{PoPDA}_\text{L}$  electrode exhibits significant capacity decay. These results at current densities of 0.2 and 1.0  $\text{A g}^{-1}$  confirm that the high-molecular-weight  $\text{PoPDA}_\text{H}$  effectively enhances electrode lifespan. Additionally, SEM images before and after 1000 cycles (Fig. S5 and S6†) demonstrate that the  $\text{PoPDA}_\text{H}$  electrode preserves its initial morphology without significant structural changes following long-term cycling. To further investigate how high molecular weight influences solubility,  $\text{PoPDA}_\text{H}$  and  $\text{PoPDA}_\text{L}$  electrodes were separately immersed in 3.0 M  $\text{Zn}(\text{CF}_3\text{SO}_3)_2$  electrolyte. The samples were then placed in a constant-temperature oven at 60 °C for one week to accelerate aging. Subsequent XRD analysis revealed that  $\text{PoPDA}_\text{H}$  exhibited minimal peak shape changes and intensity reduction, whereas  $\text{PoPDA}_\text{L}$  showed significant alterations in peak shape. These results indicate that  $\text{PoPDA}_\text{H}$  undergoes less structural degradation, which is often accompanied by dissolution, compared to  $\text{PoPDA}_\text{L}$  (Fig. S7†).

The CV curves of  $\text{PoPDA}_\text{L}$ , as shown in Fig. 4a, exhibit a pair of sharp redox peaks centered at approximately 0.58/0.67 V. These characteristics indicate a one-step redox reaction and suggest that the  $\text{Zn}^{2+}$  insertion/extraction process is predominantly governed by diffusion. This finding is consistent with previous reports and further confirms that the product obtained at room temperature is a dimer. The continuous decrease in the area of the CV curves with increasing cycle numbers indicates a decline in capacity, which is associated with the dissolution of  $\text{PoPDA}_\text{L}$  in the electrolyte.<sup>7</sup> The CV curves of  $\text{PoPDA}_\text{H}$  exhibit a pair of broader redox peaks centered at 0.41/0.61 V, which are attributed to variations in polymer chain length and micro-structure, leading to peak broadening. The high degree of overlap in the first five cycles, as shown in Fig. 4b, demonstrates the excellent redox stability of  $\text{PoPDA}_\text{H}$ .

Electrochemical kinetics were evaluated using cyclic voltammetry curves acquired at scan rates ranging from 0.1 to 1.0  $\text{mV s}^{-1}$  (Fig. 4c). As shown in Fig. 4a and d linear correlation between the logarithm of peak current and scan rate suggests that pseudocapacitive effects predominantly influence the kinetic behavior of  $\text{PoPDA}_\text{H}$  (for comprehensive fitting analysis, see ESI†). As shown in Fig. 4e, the proportion of charge storage attributed to pseudocapacitive contributions increases with scan rate, contrasting with diffusion-controlled processes where a higher pseudocapacitive contribution signifies superior rate performance (for details, see the Fig. S8†). The  $b$ -values for the principal oxidation/reduction peaks are closely matched (0.81/0.86), demonstrating high redox reversibility.<sup>39</sup> Fig. 4f displays

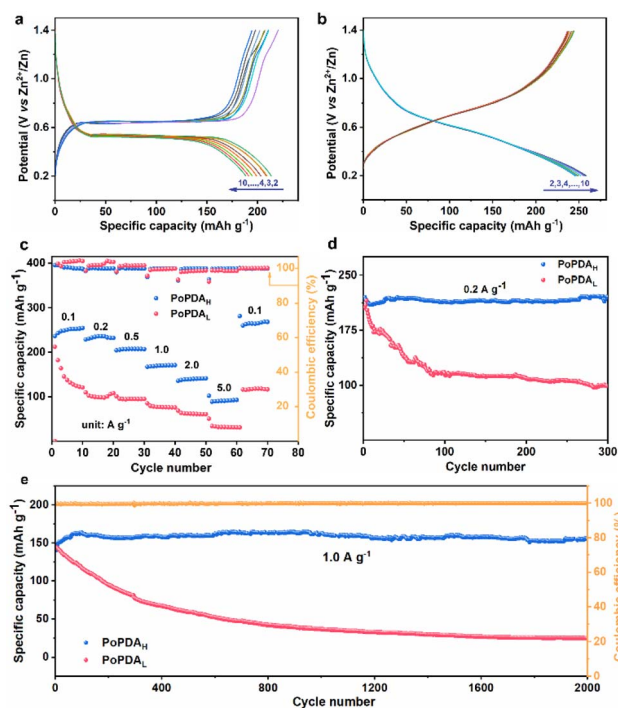


Fig. 3 (a and b) The GCD curves of  $\text{PoPDA}_\text{L}$  and  $\text{PoPDA}_\text{H}$  at 0.1  $\text{A g}^{-1}$ , (c) rate performance of  $\text{PoPDA}_\text{L}$  and  $\text{PoPDA}_\text{H}$ , (d) and (e) long-term cycle performance at 0.2  $\text{A g}^{-1}$  and 1.0  $\text{A g}^{-1}$ .



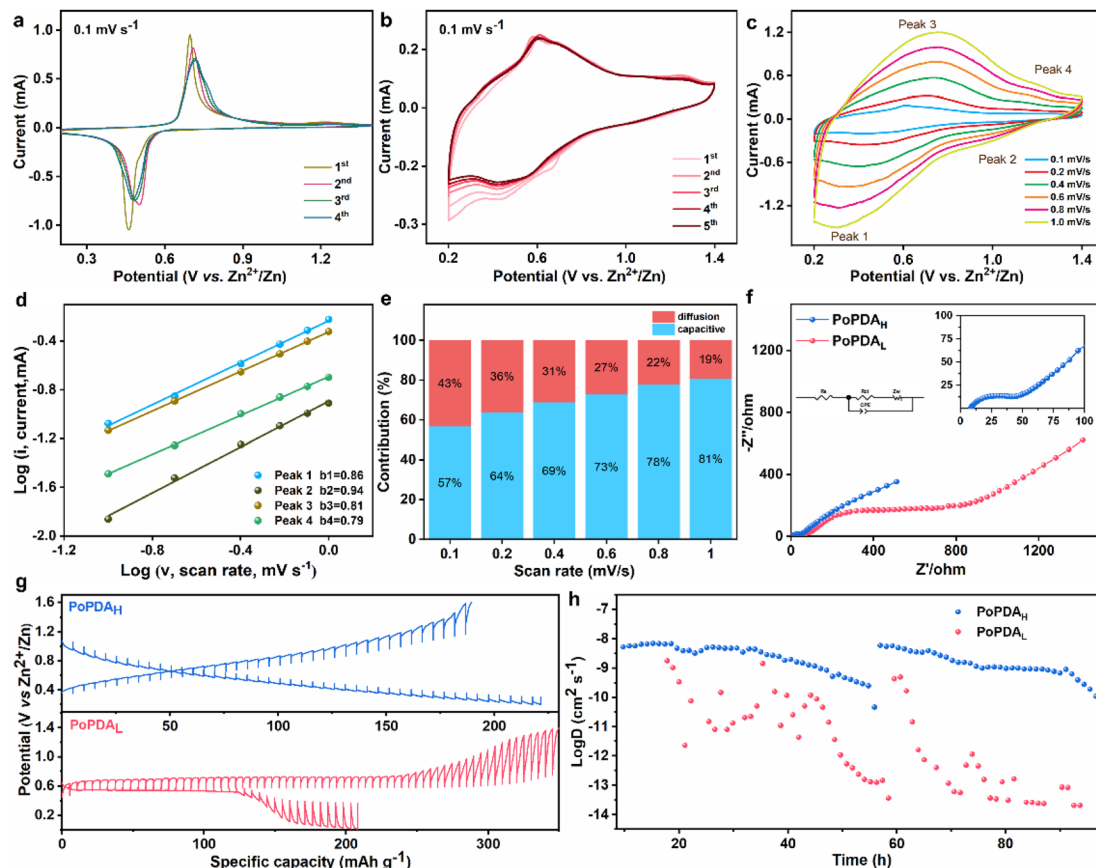


Fig. 4 CV curves of (a) PoPDA<sub>H</sub> and (b) PoPDAL at 0.1 mV s<sup>-1</sup> for the first 5 cycles, (c) PoPDA<sub>H</sub> at 0.1 to 1.0 mV s<sup>-1</sup> (d) *b* values, (e) contribution proportions of pseudocapacitive and diffusion-controlled processes, (f) Nyquist plots of PoPDA<sub>H</sub> and PoPDAL, (g) GITT curves of PoPDA<sub>H</sub> and PoPDAL, (h) the corresponding Zn<sup>2+</sup> ion diffusion coefficient (*D*).

the electrochemical impedance spectroscopy (EIS) of PoPDA<sub>H</sub> and PoPDAL electrodes after 1000 cycles, with Nyquist plots showing a semicircle in the high-frequency region (representing charge-transfer resistance) and a straight line in the low-frequency region (representing Warburg impedance). EIS data fitting indicates PoPDA<sub>H</sub> has a charge-transfer resistance ( $R_{ct}$ ) of 39.1  $\Omega$ , compared to PoPDAL's  $R_{ct}$  of 1266.7  $\Omega$ , explaining their distinct cycling stability. Additional galvanostatic intermittent titration technique (GITT) measurements were performed to examine zinc-ion diffusion kinetics (Fig. 4g). As depicted in Fig. 4h, PoPDA<sub>H</sub> exhibits an ion diffusion coefficient between  $10^{-8}$  and  $10^{-9}$  cm<sup>2</sup> s<sup>-1</sup>, significantly exceeding that of PoPDAL, demonstrating that the higher polymerization degree of PoPDA<sub>H</sub> substantially enhances ion diffusion rates. Overall, the superior kinetic behavior and structural stability of PoPDA<sub>H</sub> confer exceptional electrochemical performance.

To elucidate the underlying mechanisms in PoPDA<sub>H</sub>, *ex situ* XRD characterization was initially conducted. No Zn<sub>2</sub><sup>+</sup>(OTf)<sub>*n*</sub>(OH)<sub>2*m*-*n*</sub>·*x*H<sub>2</sub>O byproduct was detected under typical discharge conditions (Fig. 5a). Previous studies have shown that many n-type compounds, such as quinone polymers, produce Zn<sub>2</sub><sup>+</sup>(OTf)<sub>*n*</sub>(OH)<sub>2*m*-*n*</sub>·*x*H<sub>2</sub>O byproducts during the discharge process, accompanied by H<sup>+</sup> coordination.<sup>14,40</sup> This indicates

that, in this instance, only Zn<sup>2+</sup> serves as the charge carrier, with H<sup>+</sup> not contributing to the coordination process.<sup>15,16,19,41</sup>

Subsequent investigation of the charge storage mechanisms involved *ex situ* FTIR and XPS analysis. Fig. 5d-f show that the peak at 1650 cm<sup>-1</sup>, corresponding to the C=N stretching vibration, diminishes with increasing depth of discharge, and upon charging to 1.4 V, the characteristic peak intensity of the C=N double bond returns to its original state. Conversely, the peak at 1220 cm<sup>-1</sup>, corresponding to the C-N stretching vibration, intensifies with increasing depth of discharge, and upon charging to 1.4 V, the characteristic peak intensity of the C-N single bond returns to its original state. This suggests that the PoPDA<sub>H</sub> electrode undergoes a reversible Zn<sup>2+</sup> insertion and extraction process. The Zn 2p and N 1s XPS spectra of PoPDA<sub>H</sub> also confirm the reversible zincation/dezincation process during battery cycling, with the intensity of the Zn peak in the Zn 2p spectrum (Fig. 5c) evolving reversibly with Zn<sup>2+</sup> insertion and extraction. The N 1s peak in the pristine electrode downshifts to a lower binding energy of 399.4 eV from 399.9 eV during Zn<sup>2+</sup> insertion, indicating an increase in electron density. This is attributed to the electron acceptance and bonding with Zn<sup>2+</sup>, implying a reduction of -N= functional groups. In contrast, the N 1s peak returns to its original position



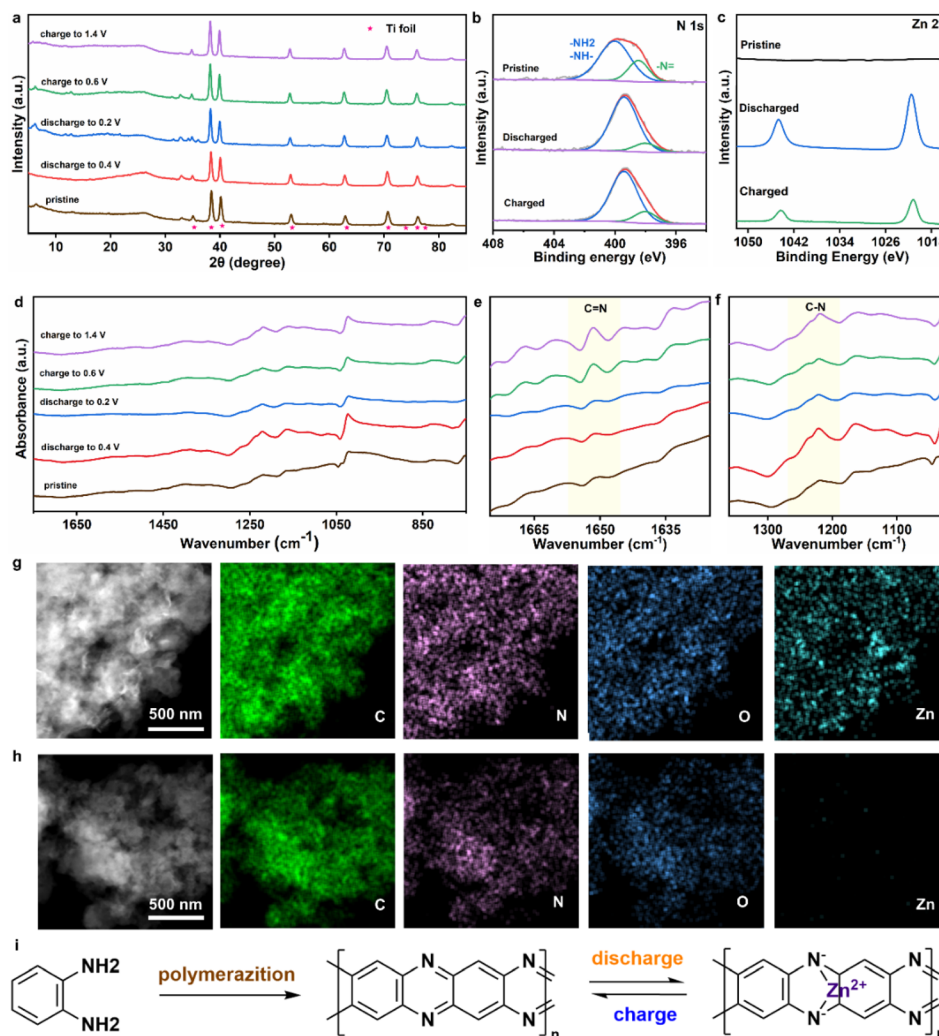


Fig. 5 (a) XRD patterns of PoPDA<sub>H</sub> cathode at different discharge and charge states, XPS spectra of (b) N 1s and (c) Zn 2p of PoPDA<sub>H</sub> cathode at pristine, fully discharged and charged state, respectively, (d–f) FTIR spectra of PoPDA<sub>H</sub> cathode at different discharge and charge states, (g) and (h) EDS mapping of C, N, O and Zn of PoPDA<sub>H</sub> cathode at fully discharged and charged state, respectively, (i) the schematic diagram of the Zn<sup>2+</sup> storage mechanism.

during discharging, which is consistent with the FTIR results (Fig. 5b). The spatial distribution of C and N elements was analyzed by EDS mapping coupled with SEM. As shown in Fig. S9,<sup>†</sup> no significant distributional alterations of these elements were detected before and after cycling. Additionally, EDS mapping combined with TEM was used to investigate the distribution of C, N, and O elements. The results presented in Fig. 5g and h indicate no substantial distributional differences between the fully discharged and fully charged samples. The weak Zn signal observed in the fully charged sample is in good agreement with the Zn 2p XPS spectra, as elaborated in the following section. These findings have been synthesized to depict the redox mechanism of PoPDA<sub>H</sub> in Fig. 5i, which exhibits characteristics of n-type organic material.

## 4 Conclusions

This study demonstrates the significant potential of high-molecular-weight poly(*o*-phenylenediamine) (PoPDA<sub>H</sub>) as

a cathode material for zinc-ion organic batteries (ZOBs). Through *in situ* chemical oxidative polymerization, PoPDA<sub>H</sub> was synthesized and exhibited remarkable electrochemical performance. It delivered a high capacity of 258 mAh g<sup>-1</sup> at 0.1 A g<sup>-1</sup> and retained 97.4% of its capacity after 2000 cycles at 1.0 A g<sup>-1</sup>. The enhanced performance is attributed to its high molecular weight and pronounced  $\pi$ - $\pi$  conjugated structure, which reduced electrolyte solubility and improved electrochemical activity. Furthermore, PoPDA<sub>H</sub> showed excellent rate capability and superior electrochemical kinetics compared to PoPDA<sub>L</sub>. The results highlight the advantages of PoPDA<sub>H</sub> in terms of production cost and synthetic simplicity, making it a promising candidate for high-performance ZOB electrode materials and advancing the development of organic electrode materials for energy storage systems.

## Data availability

The data supporting this article have been included as part of the ESI.<sup>†</sup>





## Author contributions

Yi Xu: writing – review & editing, writing – original draft, methodology, investigation, formal analysis, data curation, conceptualization. Xian-Zhong Tang: visualization, validation, supervision, methodology, funding acquisition, formal analysis, conceptualization. Xingchen Xie: writing – original draft, methodology, investigation, formal analysis, data curation, conceptualization. Ni Wang: writing – original draft, visualization, validation, supervision, funding acquisition, conceptualization. Sridhar Komarneni: writing – review & editing, writing – original draft, visualization, validation, supervision, resources, project administration, methodology, funding acquisition, conceptualization.

## Conflicts of interest

There are no conflicts to declare.

## Notes and references

- 1 L. Li, Q. Zhang, B. He, R. Pan, Z. Wang, M. Chen, Z. Wang, K. Yin, Y. Yao, L. Wei and L. Sun, Advanced Multifunctional Aqueous Rechargeable Batteries Design: From Materials and Devices to Systems, *Adv. Mater.*, 2022, **34**, 2104327.
- 2 Z. Huang, Y. Hou, T. Wang, Y. Zhao, G. Liang, X. Li, Y. Guo, Q. Yang, Z. Chen, Q. Li, L. Ma, J. Fan and C. Zhi, Manipulating anion intercalation enables a high-voltage aqueous dual ion battery, *Nat. Commun.*, 2021, **12**, 3106.
- 3 G. Li, L. Sun, S. Zhang, C. Zhang, H. Jin, K. Davey, G. Liang, S. Liu, J. Mao and Z. Guo, Developing Cathode Materials for Aqueous Zinc Ion Batteries: Challenges and Practical Prospects, *Adv. Funct. Mater.*, 2024, **34**, 2301291.
- 4 N. Zhang, J. Wang, X. Liu, P.-F. Wang, Y.-G. Liu, Y. Xie and T.-F. Yi, Towards high-performance aqueous Zn–MnO<sub>2</sub> batteries: Formation mechanism and alleviation strategies of irreversible inert phases, *Composites, Part B*, 2023, **260**, 110770.
- 5 K. Zhu and W. Yang, Vanadium-Based Cathodes for Aqueous Zinc-Ion Batteries: Mechanisms, Challenges, and Strategies, *Acc. Chem. Res.*, 2024, **57**, 2887–2900.
- 6 J. Liu, Z. Shen and C.-Z. Lu, Research progress of Prussian blue and its analogues for cathodes of aqueous zinc ion batteries, *J. Mater. Chem. A*, 2024, **12**, 2647–2672.
- 7 Q. Wang, Y. Liu and P. Chen, Phenazine-based organic cathode for aqueous zinc secondary batteries, *J. Power Sources*, 2020, **468**, 228401.
- 8 Z. Lin, H.-Y. Shi, L. Lin, X. Yang, W. Wu and X. Sun, A high capacity small molecule quinone cathode for rechargeable aqueous zinc-organic batteries, *Nat. Commun.*, 2021, **12**, 4424.
- 9 Q. Zhao, W. Huang, Z. Luo, L. Liu, Y. Lu, Y. Li, L. Li, J. Hu, H. Ma and J. Chen, High-capacity aqueous zinc batteries using sustainable quinone electrodes, *Sci. Adv.*, 2018, **4**, eaao1761.
- 10 B. Yang, Y. Ma, D. Bin, H. Lu and Y. Xia, Ultralong-Life Cathode for Aqueous Zinc-Organic Batteries *via* Pouring 9,10-Phenanthraquinone into Active Carbon, *ACS Appl. Mater. Interfaces*, 2021, **13**, 58818–58826.
- 11 G. Dawut, Y. Lu, L. Miao and J. Chen, High-performance rechargeable aqueous Zn-ion batteries with a poly(benzoquinonyl sulfide) cathode, *Inorg. Chem. Front.*, 2018, **5**, 1391–1396.
- 12 X. Wang, J. Xiao and W. Tang, Hydroquinone *versus* Pyrocatechol Pendants Twisted Conjugated Polymer Cathodes for High-Performance and Robust Aqueous Zinc-Ion Batteries, *Adv. Funct. Mater.*, 2022, **32**, 2108225.
- 13 N. Patil, J. Palma and R. Marcilla, Macromolecular Engineering of Poly(catechol) Cathodes towards High-Performance Aqueous Zinc-Polymer Batteries, *Polymers*, 2021, **13**, 1673.
- 14 T. Sun, Z.-J. Li, Y.-F. Zhi, Y.-J. Huang, H. J. Fan and Q. Zhang, Poly(2,5-Dihydroxy-1,4-Benzoquinonyl Sulfide) As an Efficient Cathode for High-Performance Aqueous Zinc-Organic Batteries, *Adv. Funct. Mater.*, 2021, **31**, 2010049.
- 15 D. Ma, H. Zhao, F. Cao, H. Zhao, J. Li, L. Wang and K. Liu, A carbonyl-rich covalent organic framework as a high-performance cathode material for aqueous rechargeable zinc-ion batteries, *Chem. Sci.*, 2022, **13**, 2385–2390.
- 16 M. Yu, N. Chandrasekhar, R. K. M. Raghupathy, K. H. Ly, H. Zhang, E. Dmitrieva, C. Liang, X. Lu, T. D. Kühne, H. Mirhosseini, I. M. Weidinger and X. Feng, A High-Rate Two-Dimensional Polyarylimide Covalent Organic Framework Anode for Aqueous Zn-Ion Energy Storage Devices, *J. Am. Chem. Soc.*, 2020, **142**, 19570–19578.
- 17 S. Zheng, D. Shi, D. Yan, Q. Wang, T. Sun, T. Ma, L. Li, D. He, Z. Tao and J. Chen, Orthoquinone-Based Covalent Organic Frameworks with Ordered Channel Structures for Ultrahigh Performance Aqueous Zinc-Organic Batteries, *Angew. Chem., Int. Ed.*, 2022, **61**, e202117511.
- 18 W. Wang, V. S. Kale, Z. Cao, S. Kandambeth, W. Zhang, J. Ming, P. T. Parvatkar, E. Abou-Hamad, O. Shekhah, L. Cavallo, M. Eddaoudi and H. N. Alshareef, Phenanthroline Covalent Organic Framework Electrodes for High-Performance Zinc-Ion Supercapattery, *ACS Energy Lett.*, 2020, **5**, 2256–2264.
- 19 H. Peng, S. Huang, V. Montes-García, D. Pakulski, H. Guo, F. Richard, X. Zhuang, P. Samorì and A. Ciesielski, Supramolecular Engineering of Cathode Materials for Aqueous Zinc-ion Energy Storage Devices: Novel Benzothiadiazole Functionalized Two-Dimensional Olefin-Linked COFs, *Angew. Chem., Int. Ed.*, 2023, **62**, e202216136.
- 20 A. Khayum M, M. Ghosh, V. Vijayakumar, A. Halder, M. Nurhuda, S. Kumar, M. Addicoat, S. Kurungot and R. Banerjee, Zinc ion interactions in a two-dimensional covalent organic framework based aqueous zinc ion battery, *Chem. Sci.*, 2019, **10**, 8889–8894.
- 21 W. Qiu, R. Zhou, L. Yang and Q. Liu, Lithium-ion rechargeable battery with petroleum coke anode and polyaniline cathode, *Solid State Ionics*, 1996, **86–88**, 903–906.
- 22 M. S. Rahmanifar, M. F. Mousavi, M. Shamsipur and H. Heli, A study on open circuit voltage reduction as a main



- drawback of Zn–polyaniline rechargeable batteries, *Synth. Met.*, 2005, **155**, 480–484.
- 23 A. Wu, E. C. Venancio and A. G. MacDiarmid, Polyaniline and polypyrrole oxygen reversible electrodes, *Synth. Met.*, 2007, **157**, 303–310.
  - 24 B. N. Grgur, V. Ristić, M. M. Gvozdenović, M. D. Maksimović and B. Z. Jugović, Polyaniline as possible anode materials for the lead acid batteries, *J. Power Sources*, 2008, **180**, 635–640.
  - 25 A. Mirmohseni and R. Solhjo, Preparation and characterization of aqueous polyaniline battery using a modified polyaniline electrode, *Eur. Polym. J.*, 2003, **39**, 219–223.
  - 26 W. Wu, H.-Y. Shi, Z. Lin, X. Yang, C. Li, L. Lin, Y. Song, D. Guo, X.-X. Liu and X. Sun, The controlled quinone introduction and conformation modification of polyaniline cathode materials for rechargeable aqueous zinc-polymer batteries, *Chem. Eng. J.*, 2021, **419**, 129659.
  - 27 F. Wan, L. Zhang, X. Wang, S. Bi, Z. Niu and J. Chen, An Aqueous Rechargeable Zinc-Organic Battery with Hybrid Mechanism, *Adv. Funct. Mater.*, 2018, **28**, 1804975.
  - 28 H.-Y. Shi, Y.-J. Ye, K. Liu, Y. Song and X. Sun, A Long-Cycle-Life Self-Doped Polyaniline Cathode for Rechargeable Aqueous Zinc Batteries, *Angew. Chem., Int. Ed.*, 2018, **57**, 16359–16363.
  - 29 S. Li, G. Zhang, G. Jing and J. Kan, Aqueous zinc–polyaniline secondary battery, *Synth. Met.*, 2008, **158**, 242–245.
  - 30 S. Zhang, S. Long, H. Li and Q. Xu, A high-capacity organic cathode based on active N atoms for aqueous zinc-ion batteries, *Chem. Eng. J.*, 2020, **400**, 125898.
  - 31 Y. Zhao, Y. Wang, Z. Zhao, J. Zhao, T. Xin, N. Wang and J. Liu, Achieving high capacity and long life of aqueous rechargeable zinc battery by using nanoporous-carbon-supported poly(1,5-naphthalenediamine) nanorods as cathode, *Energy Storage Mater.*, 2020, **28**, 64–72.
  - 32 J. Wang, Z. Zhao, Q. Weng and X. Wan, Insights on polymeric materials for the optimization of high-capacity anodes, *Composites, Part B*, 2022, **243**, 110131.
  - 33 W. Zhang, Z. Wang, C. Zhang, Y. Pang, W. Zhang and Z. Li, Construction of carbon coated spherical  $\text{Zn}_{0.71}\text{Mn}_{0.29}\text{Se}@C$  for high-performance aluminum ion batteries, *Composites, Part B*, 2024, **283**, 111661.
  - 34 Y. Zhao, Y. Huang, R. Chen, F. Wu and L. Li, Tailoring double-layer aromatic polymers with multi-active sites towards high performance aqueous Zn–organic batteries, *Mater. Horiz.*, 2021, **8**, 3124–3132.
  - 35 X. Yue, H. Liu and P. Liu, Polymer grafted on carbon nanotubes as a flexible cathode for aqueous zinc ion batteries, *Chem. Commun.*, 2019, **55**, 1647–1650.
  - 36 S. Naskar, M. Ojha, T. R. Gazi, P. Ghosal and M. Deepa, Dendrite growth inhibition in a V6O13 nanorods based non-aqueous Zn-ion battery by a scalable polycarbazole@Carbon nanotubes overlayer, *Composites, Part B*, 2023, **252**, 110516.
  - 37 W. F. Li, D. L. Peng, W. X. Huang, X. S. Zhang, Z. P. Hou, W. L. Zhang, B. X. Lin and Z. Y. Xing, Adjusting coherence length of expanded graphite by self-activation and its electrochemical implication in potassium ion battery, *Carbon*, 2023, **204**, 315–324.
  - 38 L. Cheng, C. H. Ma, W. Q. Lu, X. Wang, H. J. Yue, D. Zhang and Z. Y. Xing, A graphitized hierarchical porous carbon as an advanced cathode host for alkali metal-selenium batteries, *Chem. Eng. J.*, 2022, **433**, 133527.
  - 39 X. Wang, J. Tang and W. Tang, Manipulating Polymer Configuration to Accelerate Cation Intercalation Kinetics for High-Performance Aqueous Zinc-Ion Batteries, *Adv. Funct. Mater.*, 2022, **32**, 2200517.
  - 40 Y. Zhang, Q. Huang, Z. Song, L. Miao, Y. Lv, L. Gan and M. Liu, Fast and Stable  $\text{NH}_4^+/\text{H}^+$  Co-Coordinated Carboxyl-Rich N-Heterocyclic Cathode for High-Performance Zinc-Organic Batteries, *Adv. Funct. Mater.*, 2025, **35**, 2416415.
  - 41 K. W. Nam, S. S. Park, R. dos Reis, V. P. Dravid, H. Kim, C. A. Mirkin and J. F. Stoddart, Conductive 2D metal–organic framework for high-performance cathodes in aqueous rechargeable zinc batteries, *Nat. Commun.*, 2019, **10**, 4948.

